

Eguchi, J., et al., 2023, Limited sulfur degassing and muted environmental impact of Ontong Java Plateau lavas: Geology, <https://doi.org/10.1130/G51283.1>

## Supplemental Material

**Supplemental Text.**

**Figures S1–S5.**

**Tables S1–S8.**

## 1    **Supplementary Materials**

### 2    ***Electron Microprobe Analysis***

3            Compositional analysis of melt inclusions, host olivine, and pillow basalt glasses was  
4    conducted on the JEOL JXA-8200 Superprobe at Rutgers University. Thin sections of pillow  
5    basalt glasses contained abundant sections of fresh glass, olivine, and exposed, naturally-glassy  
6    melt inclusions (Fig. 1). Compositions were determined via wavelength dispersive spectroscopy  
7    (WDS). All phases were analyzed using a 15 kV accelerating voltage. Olivine was analyzed with  
8    a beam current of 20 nA and a focused beam while pillow basalt glass and melt inclusions were  
9    analyzed with a beam current of 10 nA and spot sizes of 2-5  $\mu\text{m}$ . Standards for olivine were  
10   olivine (Mg, Fe), orthoclase (Si), plagioclase (Al), rhodonite (Mn), magnesium chromite (Cr),  
11   diopside (Ca), ilmenite (Ti),  $\text{Ni}_2\text{SiO}_4$  (Ni), and apatite (P). Standards for pillow basalt glass and  
12   melt inclusions were albite (Na), olivine (Si), plagioclase (Al), spinel (Mg), ilmenite (Fe, Ti),  
13   rhodonite (Mn), apatite (Cl, P), troilite (S), orthoclase (K), and diopside (Ca). Mean atomic  
14   number (MAN) backgrounds were used. Counting times of 30-40 seconds were used for all  
15   elements except for Na which was analyzed with a counting time of 15 seconds. Using these  
16   conditions, analysis of basaltic standard VG-2 shows good agreement with published values,  
17   including S (Table S5). The reported detection limit for S is 60 ppm.

### 18   ***Correcting melt inclusions for post-entrapment crystallization***

19            After entrapment, melt inclusions can crystallize the host mineral along the wall and re-  
20   equilibrate with the host crystal and host magma (Danyushevsky et al., 2000). Here, we use  
21   Petrolog3 (Danyushevsky and Plechov, 2011) to account for these processes and obtain original  
22   major and trace element concentrations of the melt inclusions. To correct for post-entrapment

crystallization (PEC) and re-equilibration using Petrolog3, host olivine composition and original  $\text{FeO}_T$  of the melt inclusion at the time of entrapment is required as an input. To estimate the initial  $\text{FeO}_T$  of melts at OJP, we calculate melt compositions along the liquid line of descent in Petrolog3. We use the primary composition from Herzberg (2004) for fractional crystallization, with  $\text{FeO}_T$  adjusted to 9 wt.% as it led to better agreement with OJP glasses (Fig. S2). Olivine model used in Petrolog3 is Herzberg and O'hara (2002), with  $K_D = 0.3$ , plagioclase model is Danyushevsky (2001), clinopyroxene model is Danyushevsky (2001). Fe speciation is calculated at the FMQ buffer using the model of Kress and Carmichael (1991), and  $P = 0.001$  kbar. OJP magmas are suggested to crystallize at low  $P$  of 0.001-2 kbar (Sano and Yamashita, 2004). Figure S2 shows that the calculated liquid line of descent passes through OJP glasses measured by Roberge et al. (2004). When correcting for PEC in MIs, we set the initial  $\text{FeO}_T$  to lie along the liquid line of descent calculated for OJP magmas (Fig. S1). Uncorrected and corrected MI compositions are reported in tables S1 & S2.

### ***Calculating sulfur concentration at sulfide saturation (SCSS)***

SCSS was calculated using PySulfSat (Wieser and Gleeson, 2022), with the models of Smythe et al. (2017) and Zajacz and Tsay (2019). Calculating SCSS with the model of Smythe et al. (2017) requires melt composition,  $P$ ,  $T$ , Fe speciation, and sulfide composition. To generate the SCSS curve in Fig. 1 we use the melt composition along the Petrolog3 LLD (Fig. S2),  $P = 2$  kbar,  $T$  along the Petrolog3 LLD, Fe speciation from Petrolog3 LLD (calculated at FMQ), and sulfide  $\text{Fe}/(\text{Fe}+\text{Ni}+\text{Cu}) = 0.63$  (Ding and Dasgupta, 2018; Wieser et al., 2020). S can be dissolved as  $\text{S}^{2-}$  as well as  $\text{S}^{6+}$  depending on  $f\text{O}_2$ , and SCSS will change as  $\text{S}^{6+}/\text{S}_{\text{tot}}$  changes. In SCSS and degassing calculations, we used  $\text{S}^{6+}/\text{S}_{\text{tot}} = 0.10$  (Nash et al. 2019) assuming  $f\text{O}_2 =$  FMQ (Brounce et al., 2016) at temperature 1170 °C (from Petrolog3 LLD). The assumed  $\text{S}^{6+}/\text{S}_{\text{tot}}$

is similar to measured  $S^{6+}/S_{\text{tot}}$  of some MORBs (Lerner et al., 2021) with similar  $fO_2$  as OJP (Brounce et al., 2016). The SCSS curve in Fig. 1 and Fig S2 was generated by combining the SCSS from Smythe et al. (2017) and SCAS from Zajacz and Tsay (2019) assuming  $S^{6+}/S_{\text{tot}} = 0.10$ . SCSS is also sensitive to  $P$ , however in the  $P$  range suggested for OJP magma evolution changes to SCSS are minimal (Fig. S2).

### ***Calculating S concentrations during fractional crystallization***

S concentrations were calculated as a function of MgO along the LLD from Petrolog3. Bulk S partition coefficients were calculated using partition coefficients for clinopyroxene, plagioclase, and olivine from (Callegaro et al., 2020) and the modal abundances of minerals from the Petrolog3 LLD calculations (Fig S3).

### ***Modeling S degassing***

Closed-system degassing is modeled isothermally using Sulfur\_X (Ding et al., 2023, [https://github.com/sdecho/Sulfur\\_X](https://github.com/sdecho/Sulfur_X)). Averaged errors of modeled S in the melt from 500 simulations is 13.5%, comparable to the errors of S analysis by electron microprobe. Melt compositions are chosen to illustrate degassing of high and low MgO OJP lavas from Petrolog3 LLD at MgO ~8.9 and 7.2 wt.%, respectively. Initial  $H_2O$ ,  $CO_2$  and S for high and low MgO lavas are assumed to be 0.28 and 0.48 wt.%, 165 and 230 ppm, and 990 and 1175 ppm respectively (Fig. 2, S1, S2). Modeled  $fO_2$  is FMQ-0.2 (FMQ buffer from Frost (1991) with  $P$  correction), corresponding to initial  $Fe^{3+}/\Sigma Fe$  of 0.142 in the melt (Kress and Carmichael, 1991) and initial  $S^{6+}/\Sigma S$  of 0.095 in the melt (Nash et al., 2019). Major elements and  $fO_2$  relative to FMQ buffer are fixed through degassing (no crystallization or  $fO_2$  change due to degassing). All model inputs are listed in table S6.

## 68 *Onset of S degassing at ~150 bars*

69           In the main text we state that we consider samples with saturation  $P > 150$  bars to be  
70 undegassed with respect to S because the S degassing model predicts the onset of significant S  
71 degassing at  $P < \sim 150$  bars (Fig. 2). Additionally, data for samples collected at sites with  
72 saturation  $P > 150$  shows no observable trend of increasing S degassing efficiency with  
73 decreasing saturation  $P$  (Fig. S3) , which would be expected if S degassing was occurring. The  
74 dataset from (Reekie et al., 2019) does not report the locations of each sample, but there is a  
75 clear trend of increasing S degassing efficiency with decreasing saturation  $P$  for samples at  
76 saturation  $P < 150$  bars (Fig. S3), while there is seemingly no correlation between S degassing  
77 efficiency and saturation  $P$  for samples with saturation  $P > 150$  bars. While site 1184 shows  
78 decreasing degassing efficiency with decreasing saturation  $P$  all samples at site 1184 have very  
79 similar [S] (see Fig. 1). Although the sample at  $P \sim 100$  bars has higher degassing efficiency [S] is  
80 comparable to other samples at site 1184. This sample has a higher degassing efficiency than the  
81 other samples because it has a lower MgO, therefore the estimated  $[S]_{\text{initial}}$  is significantly higher  
82 than other samples resulting in a higher degassing efficiency. Therefore, we interpret the data as  
83 suggesting minimal degassing of S at  $P > 150$  bars. We note that a single sample at site 1187  
84 which records a significantly lower saturation  $P$  than other samples at the site ( $\sim 190$  bars) (Fig  
85 S3C) may show signs of degassing, while the higher  $P$  samples show no sign of increasing S  
86 efficiency with depth. This may suggest that in some cases S degassing may commence at  
87 slightly higher  $P$  than 150 bars. We note that a shift from  $\sim 150$  bars to  $\sim 190$  bars will not have a  
88 significant impact on our conclusions.

89           With this interpretation we set the S degassing efficiency of the samples at  $P > 150$  bars  
90 equal to zero in the discussion of the main text. In Fig. S4 we present a comparison of S

degassing efficiencies with and without prescribing S degassing efficiencies of zero at saturation  $P > 150$  bars. When we do not prescribe this filter the average S degassing efficiency of the OJP glass dataset only increases from 5% to 10%, which would still support the idea that OJP releases S much less efficiently compared to subaerial LIPs. Additionally, a set of samples from the Reekie et al. (2019) dataset is suggested to be undegassed with respect to  $\text{CO}_2$  and  $\text{H}_2\text{O}$  (Fig. S5A). The most primitive samples (highest MgO) lie around 100 ppm  $\text{CO}_2$  and 0.2 wt.%  $\text{H}_2\text{O}$ . As these samples become more fractionated (decreasing MgO) they steadily increase in  $\text{CO}_2$  and  $\text{H}_2\text{O}$  concentration, which suggests that  $\text{CO}_2$  and  $\text{H}_2\text{O}$  are undersaturated (Reekie et al., 2019). If  $\text{CO}_2$  and  $\text{H}_2\text{O}$  are undersaturated, then it is highly unlikely that S will have degassed, providing another line of reasoning for why we interpret samples with saturation  $P > 150$  bars as being undegassed with respect to S.

### ***S increase during seawater assimilation***

In the main text we suggest that the only sample that lies above our calculated SCSS values may have undergone seawater assimilation (Fig. 1). In Fig. S5 we plot  $\text{CO}_2$  vs.  $\text{H}_2\text{O}$  in OJP glasses. At around 50 ppm  $\text{CO}_2$  there is a set of data that trend off to high  $\text{H}_2\text{O}$ , while slightly decreasing in  $\text{CO}_2$  (Fig. S5). The trend of this set of glasses appears to follow an isobar of  $\text{CO}_2$ - $\text{H}_2\text{O}$  saturation pressures. We interpret this trend to result from glasses interacting with  $\text{H}_2\text{O}$ -rich seawater during eruption at a constant saturation  $P$ , which will cause  $\text{CO}_2$  and  $\text{H}_2\text{O}$  concentrations to change along an isobar to higher  $\text{H}_2\text{O}$  and lower  $\text{CO}_2$  (Fig. S5). This trend is opposite of observed trends that have been attributed to flushing by a  $\text{CO}_2$ -rich fluid (Befus et al., 2023). Figure S5C shows that the sample with the highest  $\text{H}_2\text{O}$  concentration also has the highest Cl concentrations compared to other samples at lower  $\text{H}_2\text{O}$  concentrations along the isobar. We interpret this to be the result of seawater assimilation, which will increase Cl

concentrations. Figure S5B shows that S concentrations also increase as H<sub>2</sub>O increases along the isobar, which we interpret as S addition to OJP melts from seawater interaction near the seafloor. Therefore, we suggest that the single sample which lies above the SCSS line in Fig. 1 may have high S concentrations due to interaction with seawater. Additionally, SCSS calculations are sensitive to the Fe/(Fe + Ni + Cu) ratios of the saturated sulfide. Interaction with seawater may have changed the composition of the possible coexisting sulfide which may have increased SCSS and allowed higher S concentrations for that particular sample.

#### ***Exclusion of Jackson et al. (2015) dataset for interpretation of S degassing***

Jackson et al. (2015) report data for rehomogenized melt inclusions from OJP. Their melt inclusions were collected from a crystalline section of basalt that spanned only 20 cm from Site 1187. The MgO concentrations in their rehomogenized melt inclusions extend to lower MgO concentrations than reported for glasses at site 1187 and show a trend of decreasing S concentration with decreasing MgO concentration. This trend is not observed in our new measurements of naturally glassy melt inclusions from site 1187 or in any glasses collected from a single site (Fig. S2). Additionally, CO<sub>2</sub> and H<sub>2</sub>O concentrations in the melt inclusions from Jackson et al. (2015) extend to the values lower than site 1183 and site 1184 (Fig S5), which would imply that they were entrapped in olivine at shallower depths than the depths at which site 1187 glasses were erupted. For these reasons, we exclude the Jackson et al. (2015) dataset from our discussions and interpretations on S degassing at OJP.

## 134    **References**

- 135    Befus, K.S., Ruefer, A.C., Allison, C.M., and Thompson, J.O., 2023, Quartz-hosted inclusions  
136                      and embayments reveal storage, fluxing, and ascent of the Mesa Falls Tuff, Yellowstone:  
137                      Earth and Planetary Science Letters, v. 601, p. 117909, doi:10.1016/j.epsl.2022.117909.
- 138    Brounce, M.N., Peterson, M.E., Stolper, E.M., and Eiler, J.M., 2016, Variations in Fe and S  
139                      redox states in ocean island basalts: v. 2016, p. DI13B-04.
- 140    Callegaro, S., Geraki, K., Marzoli, A., De Min, A., Maneta, V., and Baker, D.R., 2020, The  
141                      quintet completed: The partitioning of sulfur between nominally volatile-free minerals  
142                      and silicate melts: American Mineralogist, v. 105, p. 697–707, doi:10.2138/am-2020-  
143                      7188.
- 144    Danyushevsky, L.V., 2001, The effect of small amounts of H<sub>2</sub>O on crystallisation of mid-ocean  
145                      ridge and backarc basin magmas: Journal of Volcanology and Geothermal Research, v.  
146                      110, p. 265–280, doi:10.1016/S0377-0273(01)00213-X.
- 147    Danyushevsky, L.V., Della-Pasqua, F.N., and Sokolov, S., 2000, Re-equilibration of melt  
148                      inclusions trapped by magnesian olivine phenocrysts from subduction-related magmas:  
149                      Petrological implications: Contributions to Mineralogy and Petrology, v. 138, p. 68–83,  
150                      doi:10.1007/PL00007664.
- 151    Danyushevsky, L.V., and Plechov, P., 2011, Petrolog3: Integrated software for modeling  
152                      crystallization processes: Geochemistry, Geophysics, Geosystems, v. 12.
- 153    Ding, S., and Dasgupta, R., 2018, Sulfur inventory of ocean island basalt source regions  
154                      constrained by modeling the fate of sulfide during decompression melting of a  
155                      heterogeneous mantle: Journal of Petrology, v. 59, p. 1281–1308,  
156                      doi:10.1093/petrology/egy061.
- 157    Frost, B.R., 1991, Introduction to oxygen fugacity and its petrologic importance: Reviews in  
158                      Mineralogy & Geochemistry, v. 25, p. 1–9.
- 159    Herzberg, C., 2004, Partial melting below the Ontong Java Plateau: Geological Society, London,  
160                      Special Publications, v. 229, p. 179–183, doi:10.1144/GSL.SP.2004.229.01.11.
- 161    Herzberg, C., and O'hara, M.J., 2002, Plume-Associated Ultramafic Magmas of Phanerozoic  
162                      Age MODEL FOR CALCULATING: Journal of Petrology, v. 43, p. 1857–1883.
- 163    Jackson, M.G., Cabral, R.A., Rose-Koga, E.F., Koga, K.T., Price, A., Hauri, E.H., and Michael,  
164                      P., 2015, Ultra-depleted melts in olivine-hosted melt inclusions from the Ontong Java  
165                      Plateau: Chemical Geology, v. 414, p. 124–137, doi:10.1016/j.chemgeo.2015.08.014.
- 166    Kress, V.C., and Carmichael, I.S.E., 1991, The compressibility of silicate liquids containing  
167                      Fe<sub>2</sub>O<sub>3</sub> and the effect of composition, temperature, oxygen fugacity and pressure on their



redox states: *Contributions to Mineralogy and Petrology*, v. 108, p. 82–92,  
doi:10.1007/BF00307328.

Lerner, A.H., Muth, M.J., Wallace, P.J., Lanzirotti, A., Newville, M., Gaetani, G.A.,  
Chowdhury, P., and Dasgupta, R., 2021, Improving the reliability of Fe- and S-XANES  
measurements in silicate glasses: Correcting beam damage and identifying Fe-oxide  
nanolites in hydrous and anhydrous melt inclusions: *Chemical Geology*, v. 586, p.  
120610, doi:10.1016/j.chemgeo.2021.120610.

Nash, W.M., Smythe, D.J., and Wood, B.J., 2019, Compositional and temperature effects on  
sulfur speciation and solubility in silicate melts: *Earth and Planetary Science Letters*, v.  
507, p. 187–198, doi:10.1016/j.epsl.2018.12.006.

Reekie, C.D.J., Jenner, F.E., Smythe, D.J., Hauri, E.H., Bullock, E.S., and Williams, H.M., 2019,  
Sulfide resorption during crustal ascent and degassing of oceanic plateau basalts: *Nature*  
*Communications*, v. 10, p. 82, doi:10.1038/s41467-018-08001-3.

Roberge, J., White, R.V., and Wallace, P.J., 2004, Volatiles in submarine basaltic glasses from  
the Ontong Java Plateau (ODP Leg 192): implications for magmatic processes and source  
region compositions: *Geological Society, London, Special Publications*, v. 229, p. 239–  
257, doi:10.1144/GSL.SP.2004.229.01.14.

Sano, T., and Yamashita, S., 2004, Experimental petrology of basement lavas from Ocean  
Drilling Program Leg 192: implications for differentiation processes in Ontong Java  
Plateau magmas: *Geological Society, London, Special Publications*, v. 229, p. 185–218,  
doi:10.1144/GSL.SP.2004.229.01.12.

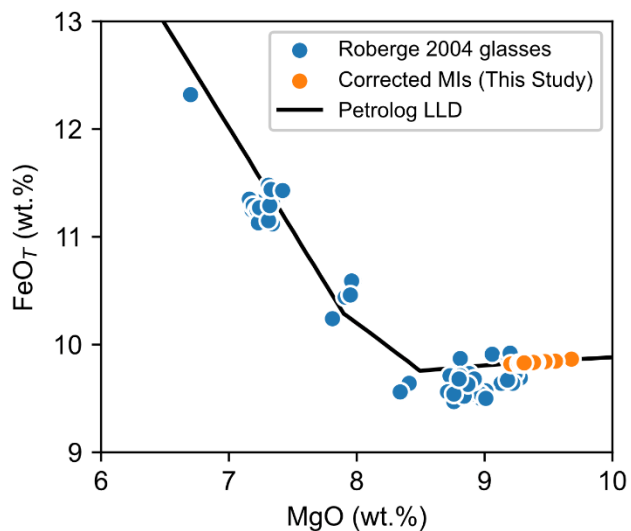
Smythe, D.J., Wood, B.J., and Kiseeva, E.S., 2017, The S content of silicate melts at sulfide  
saturation: New experiments and a model incorporating the effects of sulfide  
composition: *American Mineralogist*, v. 102, p. 795–803, doi:10.2138/am-2017-  
5800CCBY.

Wieser, P., and Gleeson, M., 2022, PySulfSat: An Open-Source Python3 Tool for modelling  
sulfide and sulfate saturation: <https://eartharxiv.org/repository/view/4624/> (accessed  
March 2023).

Wieser, P.E., Jenner, F., Edmonds, M., MacLennan, J., and Kunz, B.E., 2020, Chalcophile  
elements track the fate of sulfur at Kīlauea Volcano, Hawai'i: *Geochimica et*  
*Cosmochimica Acta*, v. 282, p. 245–275, doi:10.1016/j.gca.2020.05.018.

Zajacz, Z., and Tsay, A., 2019, An accurate model to predict sulfur concentration at anhydrite  
saturation in silicate melts: *Geochimica et Cosmochimica Acta*, v. 261, p. 288–304,  
doi:10.1016/j.gca.2019.07.007.

204 **Supplementary Figures**



205

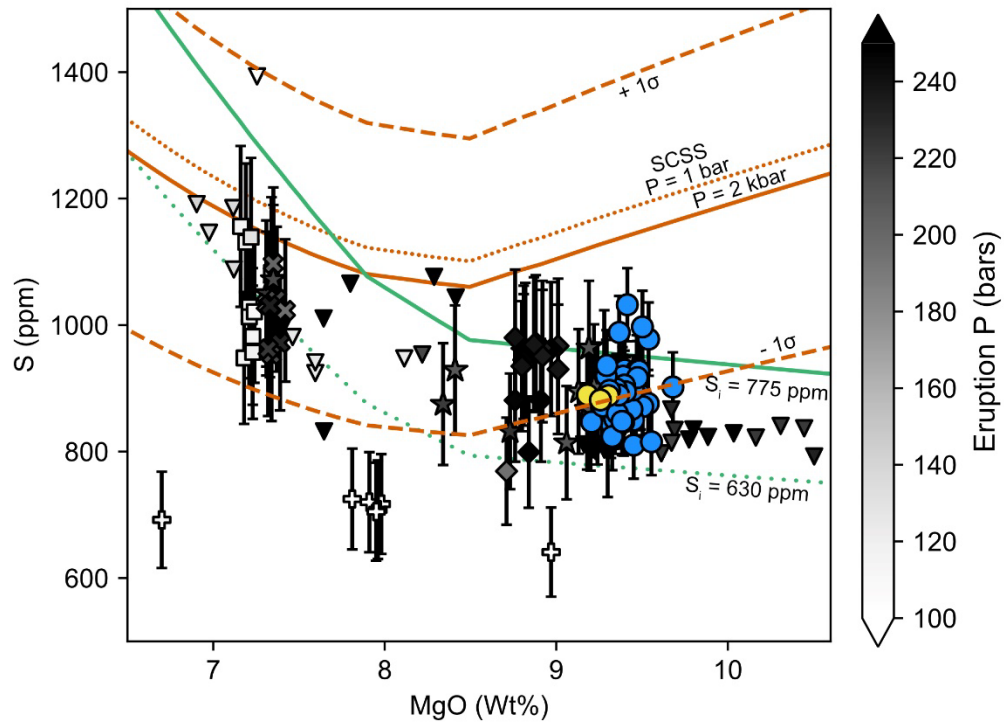
206 **Figure S1.** MgO versus FeO<sub>T</sub> in OJP glasses compared to Petrolog3 liquid line of descent. See

207 supplementary text for details on calculating LLD in Petrolog3. Initial FeO<sub>T</sub> of MIs was set to lie

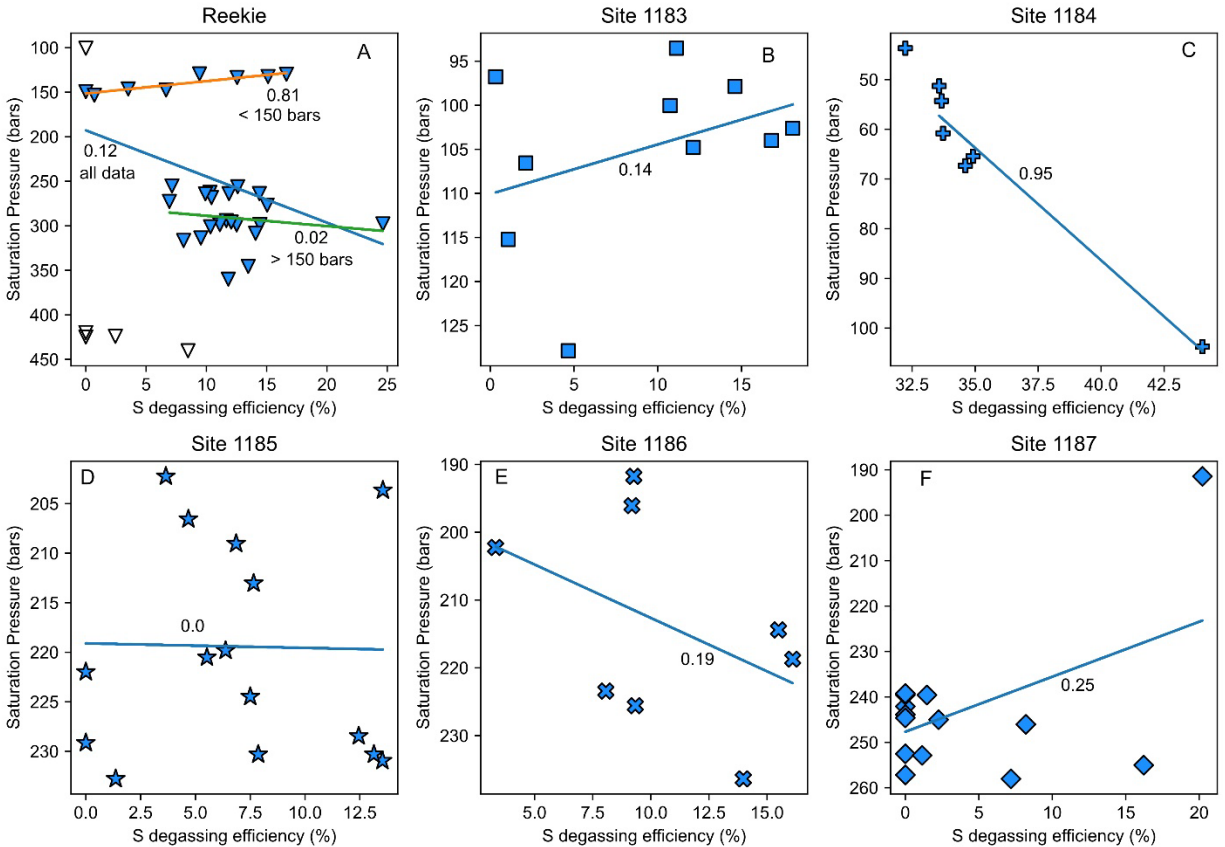
208 along the Petrolog3 LLD when correcting MIs for post-entrapment crystallization and re-

209 equilibration.

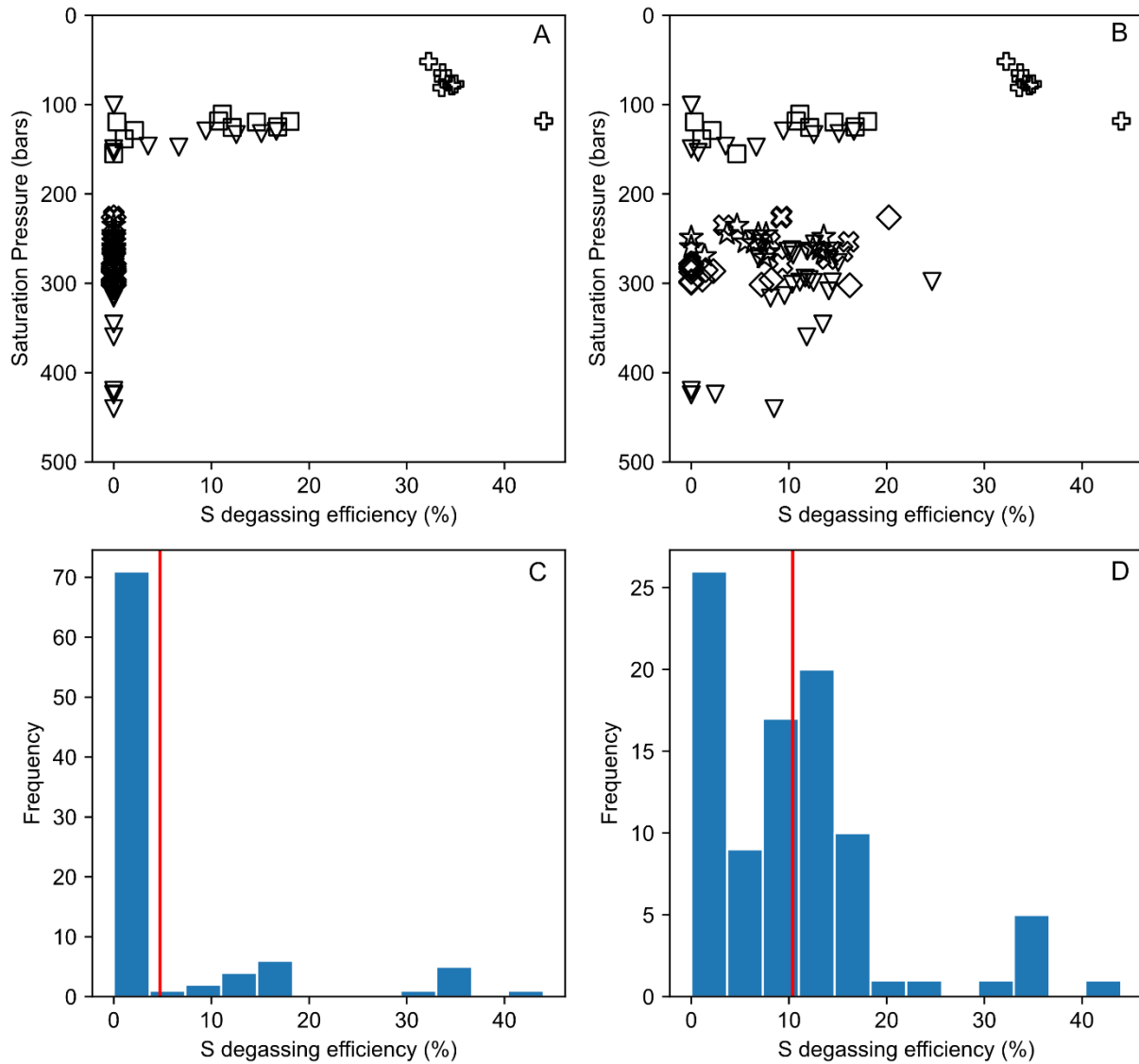
210



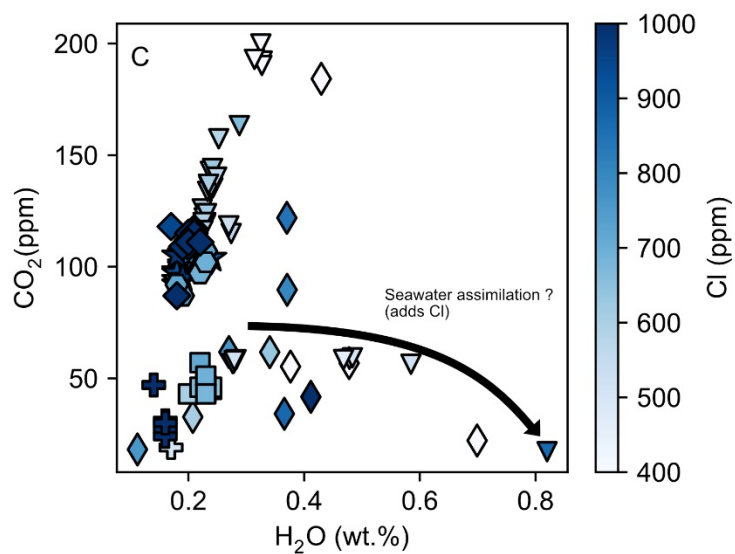
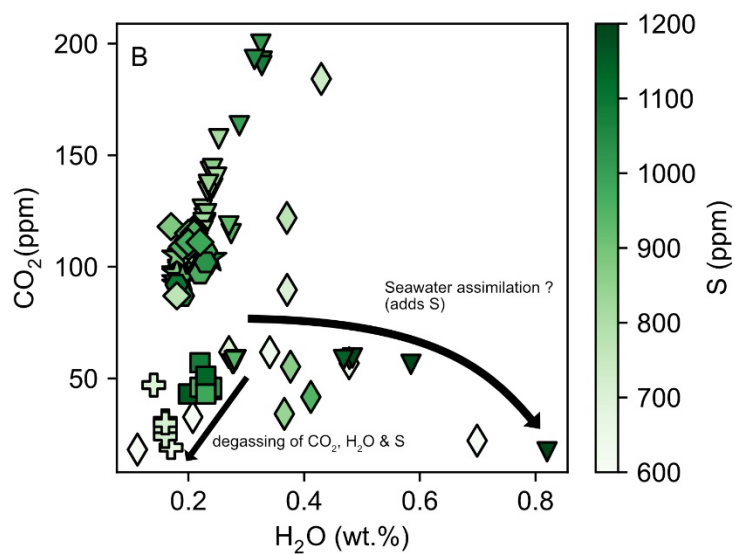
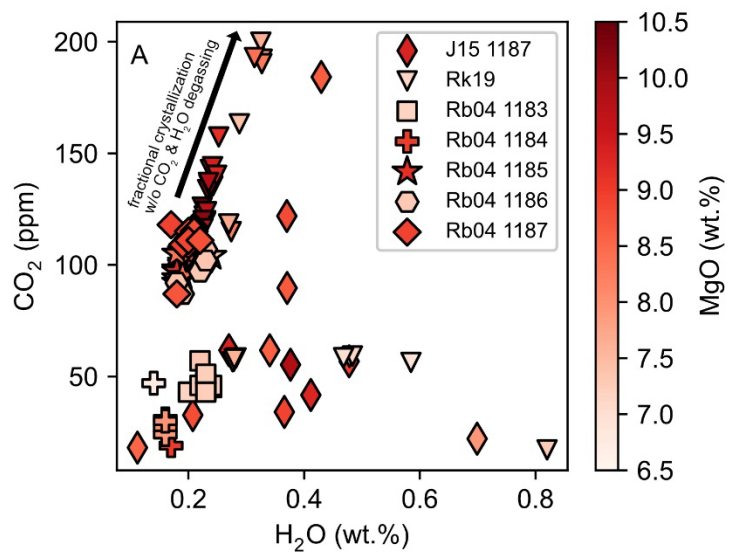
**Figure S2.** Same as Figure 1 of the main text with added  $1\sigma$  uncertainties for the calculated SCSS. For comparison SCSS at 1 bar is also plotted.



**Figure S3.** Saturation  $P$  versus S degassing efficiency for different drill sites. Lines are linear regressions of data and numbers are  $R^2$ . Trends of increasing S degassing efficiency with decreasing saturation  $P$  are only observed for sites emplaced with saturation  $P < 150$  bars. The white symbols from the Reekie et al. (2019) dataset were excluded from regressions because they were interpreted as assimilating S from seawater or being undegassed with respect to both  $\text{CO}_2$  and  $\text{H}_2\text{O}$ .



**Figure S4.** S degassing efficiencies of OJP glasses. A: Saturation  $P$  versus S degassing efficiency of OJP glasses when samples with saturation  $P > 150$  bars are inferred to be undegassed with respect to S. B: Same as panel A, except S degassing efficiencies are calculated for samples at saturation  $P > 150$  bars. C: Histogram for S degassing efficiencies when samples at saturation  $P > 150$  bars are considered to be undegassed with respect to S. D: Histogram for S degassing efficiencies when samples at saturation  $P > 150$  bars are considered to be degassed with respect to S.



231 **Figure S5.** CO<sub>2</sub> versus H<sub>2</sub>O concentrations in OJP pillow basalt glasses and MIs. A: Data color  
232 mapped to MgO concentration to show that most primitive melt compositions lie at about CO<sub>2</sub> =  
233 100 ppm and H<sub>2</sub>O = 0.2 wt.%. An array of data from the Reekie et al. (2019) dataset projects to  
234 higher CO<sub>2</sub> and H<sub>2</sub>O, which has been attributed to fractional crystallization under CO<sub>2</sub> and H<sub>2</sub>O  
235 undersaturated conditions. B: Data color mapped to S concentration. Trajectory of S degassing  
236 at low CO<sub>2</sub> and H<sub>2</sub>O is shown. Trajectory for S addition by seawater assimilation is also shown.  
237 C: Data color mapped to Cl concentration. Trajectory for Cl addition by seawater assimilation is  
238 shown. J15 = Jackson et al. (2015), Rk19 = Reekie et al. (2019), Rb04 = Roberge et al., (2004).